Radial mode breakdown of the ACAT1 fan broadband noise generation in the bypass duct using a sparse sensor array

Ulf Tapken, Maximilian Behn, Mirko Spitalny, Benjamin Pardowitz
German Aerospace Center (DLR), Institute of Propulsion Technology, Engine Acoustics Department, Berlin, Germany

I. Introduction

The detailed assessment of fan broadband noise generation in terms of the radial mode sound power was achieved in recent tests for the ACAT1 fan at the Universal Fan Facility for Acoustics (UFFA) of AneCom AeroTest[2] in Wildau, Germany, at realistic fan operating conditions up to very high characteristic frequencies of kR=85. Two methods were applied: (i) Full radial mode decomposition was realized by application of the CAAS-RMA method[1] to a combined axial and azimuthal sensor array consisting of in total 160 sensors, (ii) an estimation of the radial mode sound power content was obtained by use of the established axial wave number decomposition[7,8] (WND) method to an axial array of 60 sensors. Both analysis methods rely on different assumptions and simplifications and deliver different output data for further interpretation. It is the focus of this paper to demonstrate the methods capabilities and to make an appraisal with respect to sources of inaccuracies.

The CAAS-RMA method[1] enables the direct calculation of the sound power for each radial duct mode and thus enables new insight into the sound field generating mechanisms, e.g. with varying fan loading and fan gap. The CAAS-RMA method was verified in academic test cases, i.e. simulated measurements with sound fields synthesized by arrays of point monopole sources as well as in experiments with a loudspeaker array, which allowed a thorough investigation of the methods performance under variable degree of mode coherences against a reference technique (FSA method[3)] that fully resolves mode correlations[4]. The method was further verified in application to a low-speed fan test rig against the FSA method for a limited frequency range and compared against sound power estimation techniques using single axial and ring arrays[5]. From the earlier studie[5] it is known that the CAAS-RMA method's output is affected by superposed turbulent pressure fluctuations, by the axial flow profile and by potential mode correlations. In a study by Dougherty & Bozak[6] a combined axial line and ring array was applied and the decomposition into radial mode constituents was obtained by use of the quantitative beamforming algorithm.

The WND method implies a beamforming to an axial sensor array and produces a wave number-frequency spectrum as output. This enables the effective filtering of turbulent pressure fluctuations and the separation of the downstream and upstream traveling acoustic waves in reconstructed pressure spectra. In a subsequent step the filtered spectra can be used for an sound power estimate by assuming a certain energy distribution between radial mode orders by referring to a model such as "equal energy density per mode"[5,9] (EEDM).

The study was carried out in the frame of the EU project TurboNoiseBB and contributes to a comprehensive acoustic and aerodynamic data base[10,11] with the objective to enable the detailed characterization of the fan broadband noise generation and propagation mechanisms[12-16]. The ACAT1 fan was operated in two rotor-stator configurations at various shaft speeds on two working lines, among this the acoustic certification points. Before execution of the mode analysis the tonal and broadband components were separated by application of cyclostationary analysis[17]. For the CAAS-RMA method the impact of the axial flow profile is explicitly evaluated by consideration of the appropriate mode base functions that are derived with help of a numerical solver.

II. Fan test rig and measurement setup

Figure 1 gives an overview of the UFFA rig. Some details of the design and measurement capabilities are described in more detail in References 2 and 16. The UFFA is of a modular construction that allows rapid test bed changes to the total LP fan system including the intake, fan, outlet guide vanes (OGVs) and bypass duct. Maintaining the large scale of the fan rig allows engine, duct and acoustic liner components to be tested with

confidence with regard to their performance at full scale. The modular fan rig fan diameter is 34 inches and is powered by an 18MW Motor.

The aerodynamic and noise database presented here was obtained at AneCom AeroTest during a test campaign carried out in the spring of 2018. The tests were conducted on the ACAT1 fan, which is a transonic fan with a design pressure ratio of about 1.42 corresponding to a bypass-ratio of around 8. The rotor has 20 blades. Both the stator (bypass) and the ESS (core) have 44 vanes. Two variants of rotor-stator spacing were realized. For a short gap (SG) configuration the spacing corresponded to approximately 1.5 rotor axial chord, while it reached approximately 4 rotor axial chords for the long gap (LG) configuration. The tests were conducted during several campaigns of measurement spread over several weeks. The modification of the rotor-stator spacing necessitated to disassemble part of the rig. Each build was characterized from a performance, aerodynamic and acoustic point of view at several operating points distributed along two working lines, so-called Sea Level Static (SLS) and Low Noise (LN), cp. Figure 2. The lower (LN) working line was obtained by opening the throttle located at the exit of the bypass duct.

The acoustic instrumentation that is considered in this paper is depicted in Figure 1. Only the signals of the linear array AX1 in the bypass section and the signals of the circumferential mode detection ring CMD3, both located in the bypass section, were exploited. The array AX1 was equipped with 60 microphones mounted flush with the wall at the outer casing. The sensors were positioned in a single axial line with equidistant spacing of 13.5 mm at 0° circumferential position (the available traverse of the duct section was not used during the measurement campaign). The sensor array was optimized by Tapken et al[2] for a radial mode decomposition of fan tones up to characteristic frequencies of Helmholtz number kR=85. G.R.A.S. condenser microphones consisting of preamplifier type 26AR and capsule type 40BP were used. The circumferential CMD3 array was equipped with 100 Endevco sensors in a non-equidistant spacing. The sparse arrangement was optimized by Rademaker[18] et al for an analysis in the azimuthal mode range up to m=±79.

The sensors of the CMD3 and AX1 array were recorded together with rotor shaft trigger signals by DLR on a NI-PXI data acquisition system with a sampling frequency of 100 kHz and with 30 s duration for each test point. A known phase shift of 180° between the Endevco sensors and the G.R.A.S. microphones is considered by an adequate adjustment of the sensor transfer functions to enable the application of analysis techniques with a combined CMD3-AX1 array.

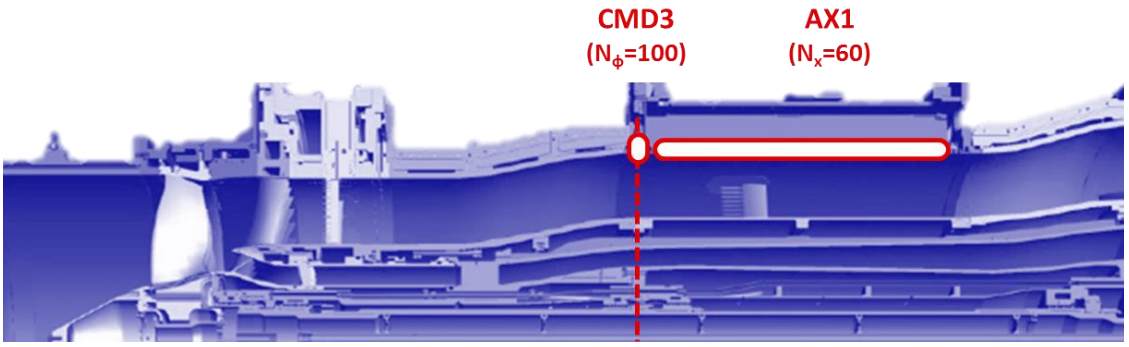

Figure 1: Aerodynamic and acoustic instrumentation used at the UFFA rig. In the bypass nozzle equivalent plane the sound field was detected by the circular sensor array CMD3 and the axial sensor array AX1.

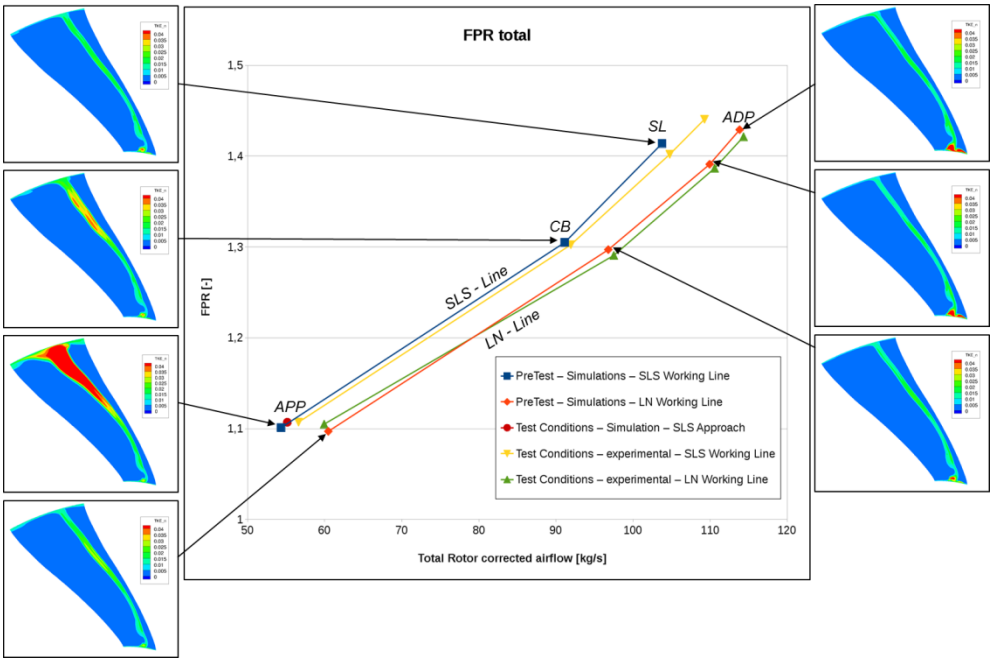

Figure 2: Performance map of the ACAT1 fan. The fan was operated at four shaft speeds on two working lines. The color maps show for illustration the distribution of normalized turbulence kinetic energy on a cross section downstream of the rotor[12].

III. Applied mode analysis methods

A. Description of sound field in the flow duct

The sound field within the duct is described as a superposition of an infinite number of modes. Under the constraints of incompressible and isentropic flow, constant axial mean flow profile, stationary mean temperature and density, the solution of the convective Helmholtz equation is given in cylindrical coordinates by a linear superposition of modal terms as follows:

$$p(x,r,\phi) = \sum_{m=-\infty}^{\infty} \sum_{n=0}^{\infty} \left(A_{mn}^{+} e^{ik_{mn}^{+}x} + A_{mn}^{-} e^{ik_{mn}^{-}x} \right) f_{mn}(r) e^{im\phi}. \tag{1}$$

Here $A_{mn}^{\pm}$ denote the complex amplitudes, $f_{mn}(r)$ the radial mode shape function and $k_{mn}^{\pm}$ the axial wave numbers of the mode with the azimuthal order m and the radial order n for propagation in and against flow direction, respectively. In case of hard-wall acoustic boundary conditions, the modes form an orthogonal eigensystem. The amplitudes of the individual modes depend on the physics of the sound generation. For tonal noise, the modes are correlated with the source and with each other. In the case of broadband noise, one can assume – as the sound energy is propagated in different modes along the duct – a given point-to-point coherence in space as well as for short periods of time, which are too short to be captured experimentally. Therefore, the only possibility to model broadband noise is by a statistical description in terms of mean values and spatial cross-correlation. In the following is assumed that the pressure time-series are time-averaged for a suitably long period to provide an invariant mean broadband noise sound field with statistical evidence, which is characteristically linked with the sound source mechanism. The analysis requires simultaneous acoustic pressure measurements at all sensor locations during a finite time interval of length T. Modes are only defined in a narrow frequency band domain. A Fourier Transform over the time interval T delivers the cross spectrum for each pair of measurement positions (x, r, ϕ) and (x_0; r_0; ϕ_0) and for each frequency component of interest

$$S_{pp'} = \langle p(x,r,\phi)\, p^*(x',r',\phi') \rangle = \lim_{T\to\infty} E\left\{ \frac{1}{T} p(x,r,\phi)\, p^*(x',r',\phi') \right\}. \tag{2}$$

B. Axial wave number decomposition (WND method)

The axial wave number decomposition (WND) technique is described in detail in references 7 and 8, where it is also referred to as axial beamformer technique. The WND method enables the separation of hydrodynamic pressure fluctuations from the acoustic pressure fluctuations propagating up- and downstream, respectively. The technique requires an axial line of sensors. The cross spectra of all possible sensor combinations $S_{j,k} = p(\varphi_j, \omega)p(\varphi_k, \omega)^*$ are calculated and combined in the cross spectral matrix S_{pp}. The contribution of each wave number component of interest is determined by multiplication with the normalized vector $\hat{g}_x$ of axial transfer functions and thereby yielding the mean squared pressure of the respective wave number component $\langle p^2(k_x)\rangle = \hat{g}_x^* S_{pp} \hat{g}_x$. The mean squared pressure of the up- resp. downstream propagating acoustic components is calculated by integration over the wavenumber domains from $kM_x/(1-M_x^2)$ to $k/(1 \mp M_x)$, where the upper sign considers the upstream propagating components and the lower sign is associated with the downstream propagating components. For this wavenumber filtering it is assumed that the underlying acoustic modes are mutually incoherent. The respective mean squared pressures are then used as input to the sound power estimation method, which refers to an assumption regarding the distribution of sound power among the different radial modes. In this study the model 'equal energy density per mode' is applied, as described in reference 5:

$$\langle \bar{P}_{WND}^{\pm} \rangle = \frac{\pi R^2}{\rho c}(1-M_x^2)^2 \frac{\sum_{m,n}|\alpha_{mn}|^2}{\sum_{m,n}|\alpha_{mn}|^2 |f_{mn(R)}|^2} \frac{\left(\sum_{m,n}\frac{\alpha_{mn}}{(1\mp\alpha_{mn}M_x)}\right) {p_{acou}^{\pm}}^2}{\left(\sum_{m,n}(1\mp\alpha_{mn}M_x)\right)}. \quad (3)$$

C. Radial mode analysis applied to combined axial and azimuthal sensor array (CAAS-RMA method)

The CAAS method is described in detail in reference 4. It evaluates the cross spectral densities that are calculated for the sensors of the ring individually with each sensor of the axial line according to equation (2) and stores them into the vectors $\boldsymbol{S}_{p_o p_l(x_j)}$. The radial mode analysis is executed in two steps: First an azimuthal mode decomposition is performed, in the second step the expected values of the squared mode amplitudes $\langle |A_{mn}^{\pm}|^2 \rangle$ of the downstream and upstream propagating radial modes are determined by a least-square fit individually for each order m.

For the azimuthal mode decomposition a Compressed Sensing approach is taken by applying the EOMP algorithm[10], which solves the following minimization problem:

$$\boldsymbol{a}_m(x_j) = \text{argmin}_{\boldsymbol{a}\in\mathbb{C}^{N_m}} \left\|\boldsymbol{a}_m(x_j)\right\|_1 \text{ subject to } \left\|\boldsymbol{S}_{p_o p_l(x_j)} - \boldsymbol{W}_{AMA}\boldsymbol{a}_m(x_j)\right\|_2 < \varepsilon, \quad (4)$$

with the azimuthal mode transfer matrix $\boldsymbol{W}_{AMA}$, assumed noise energy ε and the vectors of azimuthal mode amplitudes $\boldsymbol{a}_m(x_j)$ for each axial position. This procedure is particularly suitable regarding the non-uniform sensor arrangement and the analysis of subsampled modal fields, i.e. the number of reconstructed mode amplitudes is larger than the number of sensors. A particularity of the CAAS method is that the azimuthal mode decomposition in the first analysis step is performed on the vector of cross-spectra between the sensors of the ring and the individual sensors of the axial line array leading to a similar formulation as for the analysis of tonal components. A possible restriction of this approach lies in insufficient sparsity of respective azimuthal mode spectra, which can reduce the accuracy of the Compressed Sensing method. In contrast, the described issue of insufficient sparsity of broadband mode spectra does not occur for the extension of the Compressed Sensing method using the complete cross-spectral matrix as discussed in reference 10.

For the second step the calculated azimuthal mode spectra are combined to vectors $\boldsymbol{S}_{a(x_j),m}$ for the individual mode orders. The decomposition of the azimuthal mode spectra into the radial mode constituents is performed through solving the following minimization problem:

$$\boldsymbol{a}_{mn} = \text{argmin}_{\boldsymbol{a}_{mn}\in\boldsymbol{R}^{2N_n}} \left\|\boldsymbol{S}_{a(x_j),m} - \boldsymbol{W}_{RMA,m}\boldsymbol{a}_{mn}\right\|_2 \text{ subject to } \boldsymbol{a}_{mn,i} = |A_{mi}|^2 \geq 0, \quad (5)$$

with the radial mode transfer matrix $\boldsymbol{W}_{RMA,m}$ and the vectors of squared radial mode amplitudes $\boldsymbol{a}_{mn}$ for the respective azimuthal mode orders. The squared mode amplitudes are determined under a positivity constraint, which is guaranteed by application of a non-negative least squares (NNLS) solver[18].

The sound power carried by each individual mode can be calculated as

$$\left\langle P_{mn}^{\pm} \right\rangle = \frac{\pi R^2}{\rho c} \frac{\alpha_{mn}\left(1-M_x^2\right)^2}{\left(1 \mp \alpha_{mn} M_x\right)^2} \left\langle \left|A_{mn}^{\pm}\right|^2 \right\rangle \quad (6)$$

The CAAS method requires the assumption that all modes are fully uncorrelated. It was shown in reference 4 by simulated measurements using regular ring and axial line array geometries that in the case of fulfilled assumption the analysis is very accurate compared to the reference FSA method (resolving all mode correlations on a regular measurement grid), but if partially correlated modes are present deviations occur, which increase with increasing degree of mode coherences. For turbomachinery broadband noise it is a common assumption that all modes are fully uncorrelated, which constitutes the basis for the application in the present study.

D. Derivation of radial mode base functions under consideration of axial flow profile

The radial mode base functions and axial wave numbers under consideration of the axial flow profiles are determined by solving an extended eigenvalue problem. This is based on the linearized Euler equations in cylindrical coordinates with the assumption of harmonic base functions and hard wall boundary conditions. A radial dependency of the axial flow profile is allowed. The resulting, extended, eigenvalue problem is solved on a Chebyshev discretization. This methodology has been introduced by Kousen[19]. The implementation used here by DLR has been described in detail by Weckmüller et al.[20].

The sound power calculation has to be consistent with the solution of the extended eigenvalue problem as well. As the mode base functions are not necessarily orthogonal, as has been shown by Atassi[21], the calculation of the total sound power is given by:

$$P = Re\left\{\sum_{n=0}^{\infty}\sum_{p=0}^{\infty} A_n^* A_p w_{np}\right\}, \quad (7)$$

where w_{np} is a weighting factor for each combination of radial mode amplitudes np. The weighting factors can be derived from the formulation of the acoustic intensity given by Morfey[22]. The resulting formulation is given as:

$$w_{np} = \pi e^{i\left(k_{x,n}-k_{x,p}\right)x} \int_{\eta R}^{R} \left[\left(1+\frac{\bar{u}^2}{c^2}\right)\hat{p}_n^*\hat{u}_p + \frac{\bar{u}}{\bar{\rho}c^2}\hat{p}_n^*\hat{p}_p + \bar{\rho}\bar{u}\hat{u}_n^*\hat{u}_p\right] r dr. \quad (8)$$

In this equation $\hat{p}$ stands for the acoustic pressure and $\hat{u}$ for the acoustic velocity. Steady mean flow values are indicated by the bar. The hub to tip ratio is given by η.

IV. Separation of broadband noise components by cyclostationary analysis

Before the application of the mode analysis methods the tonal and broadband components of all measured sensor signals were separated with help of the cyclostationary analysis described in reference 16. For this analysis the measured time series are resampled with regard to the rotor shaft trigger. After resampling, the pressure signal *p(t)* is separated in blocks of each 16 rotor revolutions. The ensemble average of these blocks yields the rotor-locked signal *s(t)*, which can be interpreted as the tonal signal components. Under the assumption of cyclostationarity[23], the residual signal $r(t) = p(t) - s(t)$ contains the broadband signal components, whose phase fluctuates randomly with the rotor revolutions. The broadband signal is second-order cyclostationary (CyS2) and the tonal signal comprises first-order cyclostationarity. The result of the cyclostationary analysis is shown exemplarily in Figure 3 for two test points, i.e. Approach SLS and Cutback SLS, measured in short fan gap configuration. Depicted are the mean power spectral densities (PSD) measured by the linear array AX1. The blue curve describes the result of a quasi-stationary analysis using the Welch method, in which resampling is omitted. In the spectrum the BPF harmonics can clearly be identified at the multiples of engine order (EO) 20. Particularly at higher shaft speeds secondary tonal components become visible at other engine order. The red curves represent the filtered broadband signals (CyS2 components). They almost exactly reproduce the quasi-stationary spectrum beyond the engine orders. It should be noted that at the BPF harmonics the level of the broadband noise components is significantly higher compared to the adjacent frequency bands, however, this is not observed for the other integer engine order. For the subsequent analyses only the second order cyclostationary signal components of all CMD3 and AX1 sensors were used.

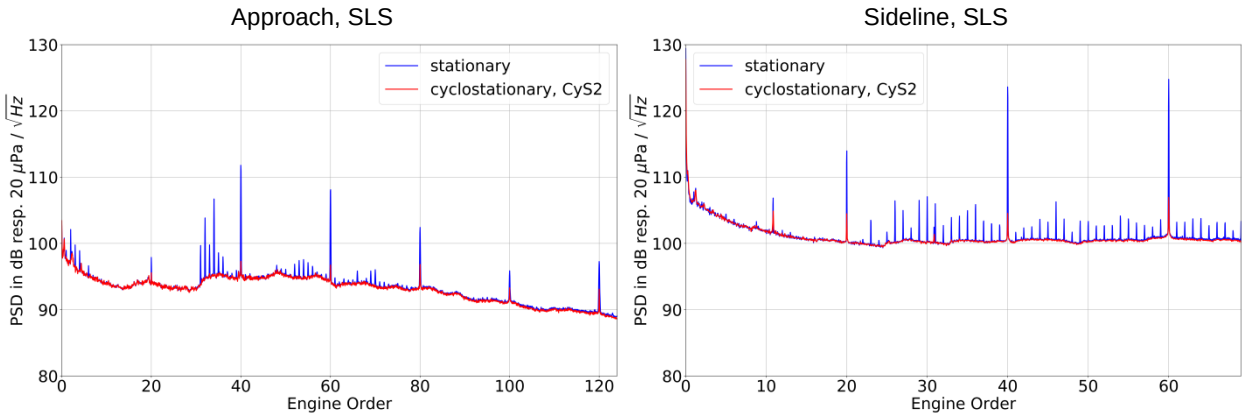

Figure 3: Tonal and broadband signal components separated by application of cyclostationary analysis with respect to the rotor shaft trigger (mean spectra measured by axial sensor array AX1).

V. Mode analysis by application of WND method

In Figure 4 the results of the WND analyses applied to sensor array AX1 are depicted for the same test points as before, i.e. Approach SLS and Sideline SLS, measured in short fan gap configuration. Displayed are the levels of pressure waves traveling with different axial phase velocities in the bypass duct. Three dominant regions can be identified in both cases: two regions extending into the positive wave number domain and one region extending into the negative wave number domain. On basis of the wave numbers they can be assigned to either convective pressure waves or downstream respectively upstream propagating pressure waves[7]. The bounds of the acoustic domain are marked by the wave numbers of the upstream and downstream traveling plane waves. An analytic approximation assuming a constant flow velocity profile is applied. It can be seen that these bounds do not exactly match the determined wave number-frequency spectra for the downstream propagating modes. This mismatch results from deviations of the actual wave numbers due to the influence of boundary layers (see Ch. VII) and the mainlobe width of the axial wave number decomposition.

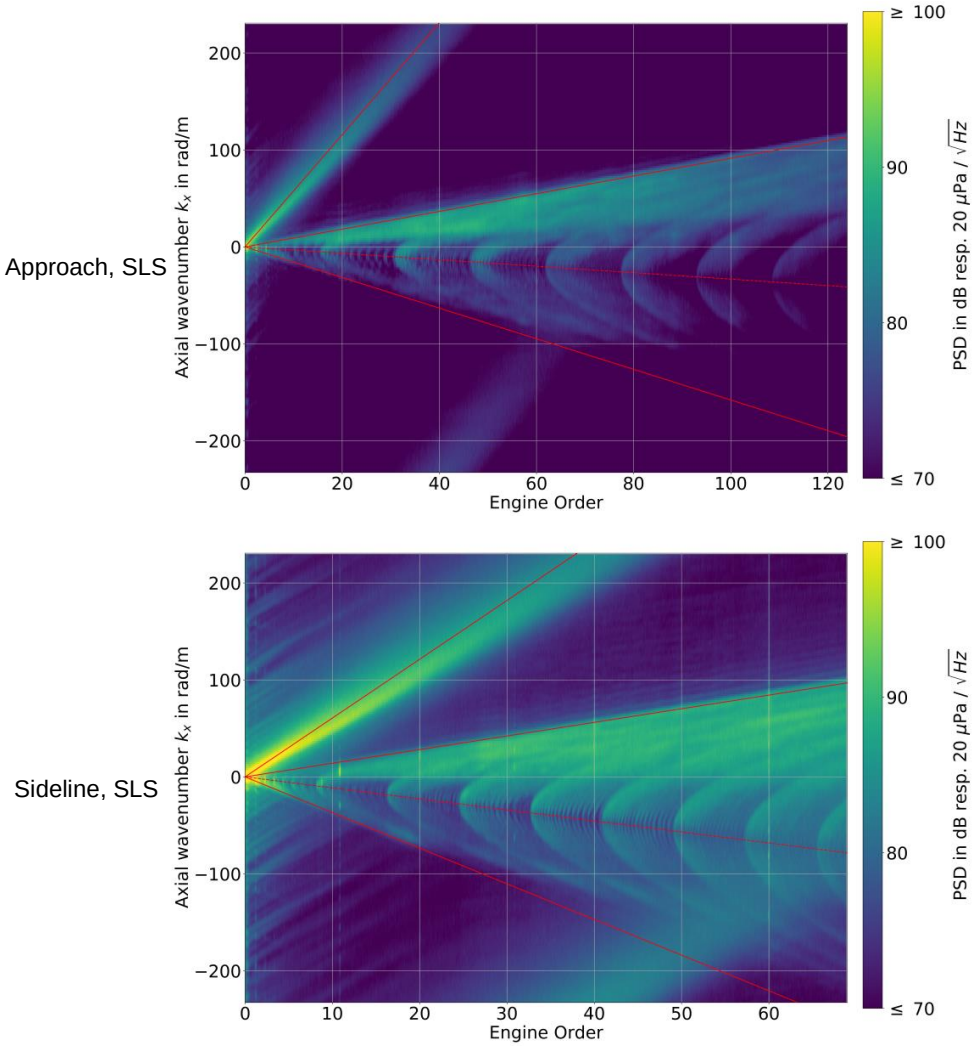

Figure 4: Axial wave number spectra showing the contribution of downstream and upstream propagating modes and of the turbulent pressure fluctuations to the pressure field detected by the axial sensor array AX1.

With help of integration over the respective wave number domains PSD spectra of the different components can be obtained if the transform is limited to the wave number region of interest. The aim of the filtering process is to get on the one hand an acoustic PSD unbiased from turbulent perturbations. On the other hand, the ratio of the turbulent pressure fluctuations to the acoustic fluctuations can be assessed. The result of the filtering process is visualized in Figure 5. The turbulent pressure fluctuations dominate the unfiltered total spectrum in the Approach SLS case up to EO 20 and in the Sideline SLS case up to EO 25. Above these frequencies the spectra are clearly dominated by the downstream traveling acoustic modes. The spectrum of the turbulent fluctuations is affected by the before-mentioned mismatch between the visible wave number boundary of the downstream traveling acoustic modes and the applied approximation in the way that the integrated spectrum is increased by the mismatched portion of the acoustic spectrum. In return, the acoustic spectrum is reduced by approximately 0.3 dB. The sound power transported by the acoustic modes is estimated using the approach described in III.B and is displayed in comparison for different test cases in Figure 13.

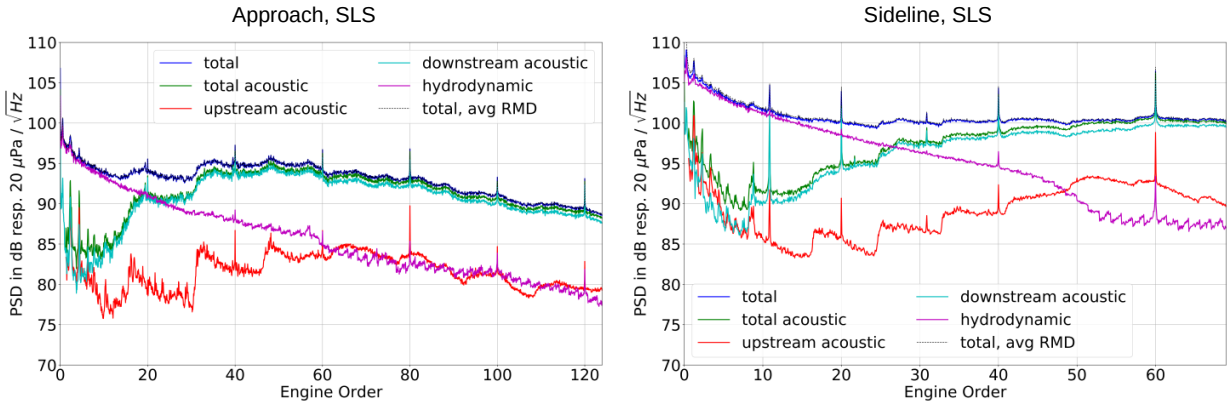

Figure 5: PSD of downstream and upstream propagating modes and of the turbulent pressure fluctuations reconstructed from the axial wave number spectra shown in Figure 4.

VI. Mode analysis by application of CAAS-RMA method

In contrast to the WND method the CAAS radial mode decomposition method determines the sound power carried by the individual acoustic modes explicitly. This is illustrated in Figure 6 for two test points measured at approach condition with different fan throttling. Depicted are the sound power level of radial mode order n=0 to n=3 in separate diagrams against frequency and azimuthal mode order m. At SLS condition large mode-frequency bands of elevated levels can be identified in particular for radial order n=0 up to engine order 60. It can be assumed that they are associated with the much larger turbulent kinetic energy of the rotor wakes, which is displayed in Figure 2 and was predicted by RANS calculations[12]. Regarding the overall mean distribution of the sound power over the radial order, the frequency band up to EO 60 is clearly dominated by radial order n=0. At higher frequency bands the contribution of the radial order converges to the same order, although there is some variation depending on the azimuthal mode order.

The diagrams in Figure 7 show the sound power cumulated over all radial order for both approach test points but in additional comparison with the long fan gap configuration. Interestingly for both fan throttle settings the same small mode-frequency band of elevated level can be found around EO 80 and m=8 in the short gap configuration, respectively around EO 75 and m=10 in the long gap configuration. This gives an impression of the validity of the CAAS method. The variation of the large dominant regions up to EO 80 in both short fan gap SLS cases can be ascribed to the different expansion of the rotor wakes. Obviously the more expanded rotor wake causes a stronger mode excitation at EO 20 to 40, but weaker mode excitation at EO 40 to 80. In all cases significant more sound power is transported by modes of positive azimuthal mode orders. A similar trend can be found for the sideline operating point test cases depicted in Figure 8 for the short gap variant. It should be noted that due to the higher rotational speed the analysis could be carried out only up to EO 68. Obviously no elevated sound power bands are found at engine order lower than EO 25. This must not be attributed to the fan noise sources, since just up to this frequency the turbulent pressure fluctuations that are not explicitly filtered out by the CAAS-RMA method dominate over the acoustic waves, as shown in the right diagram of Figure 5 and further discussed in the following sections.

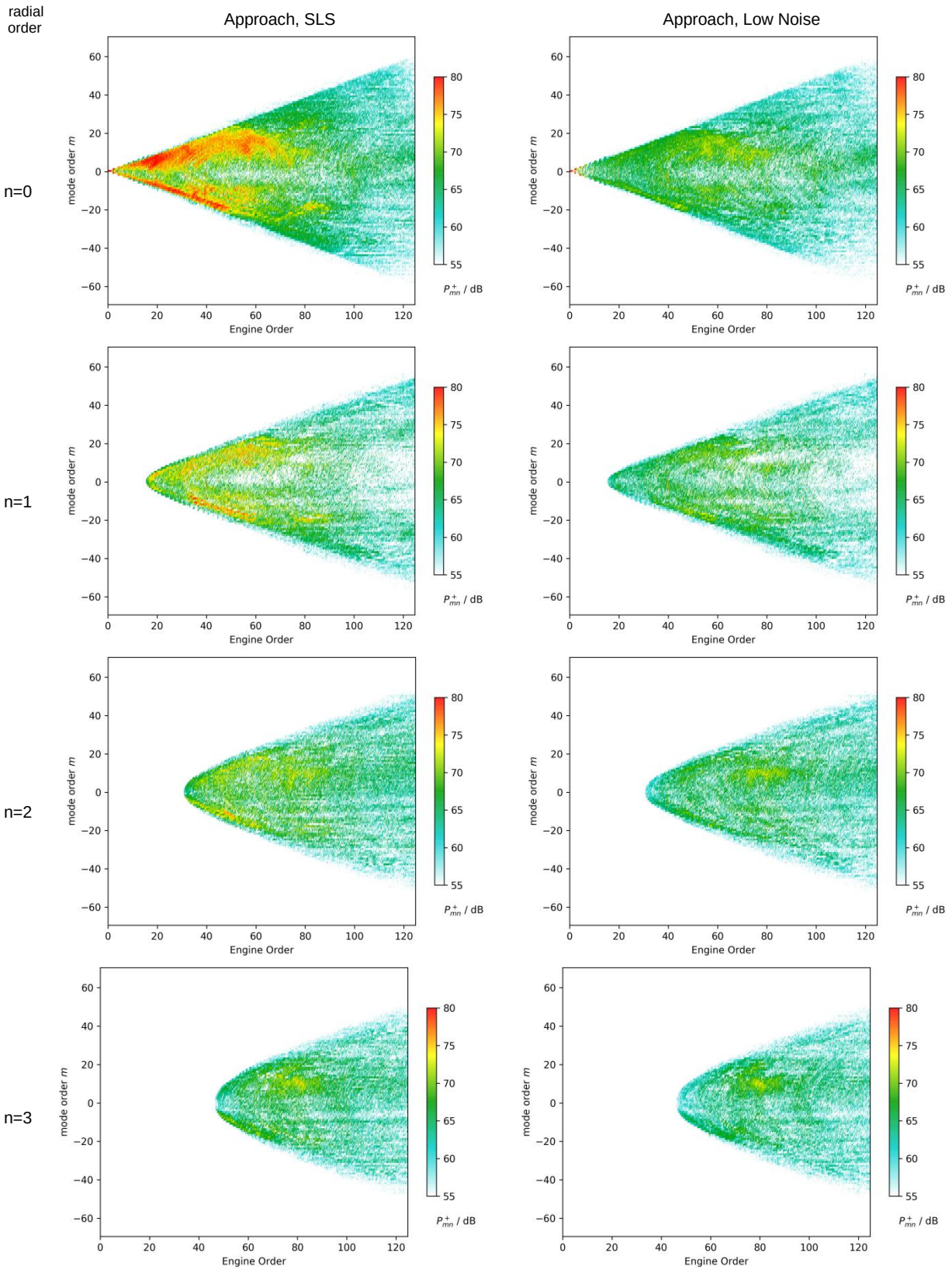

Figure 6: Sound power level of downstream propagating modes of radial order n=0 to n=3 for approach condition with two different fan throttling (data is plotted as PSD in dB resp. 10^{-12} W/Hz).

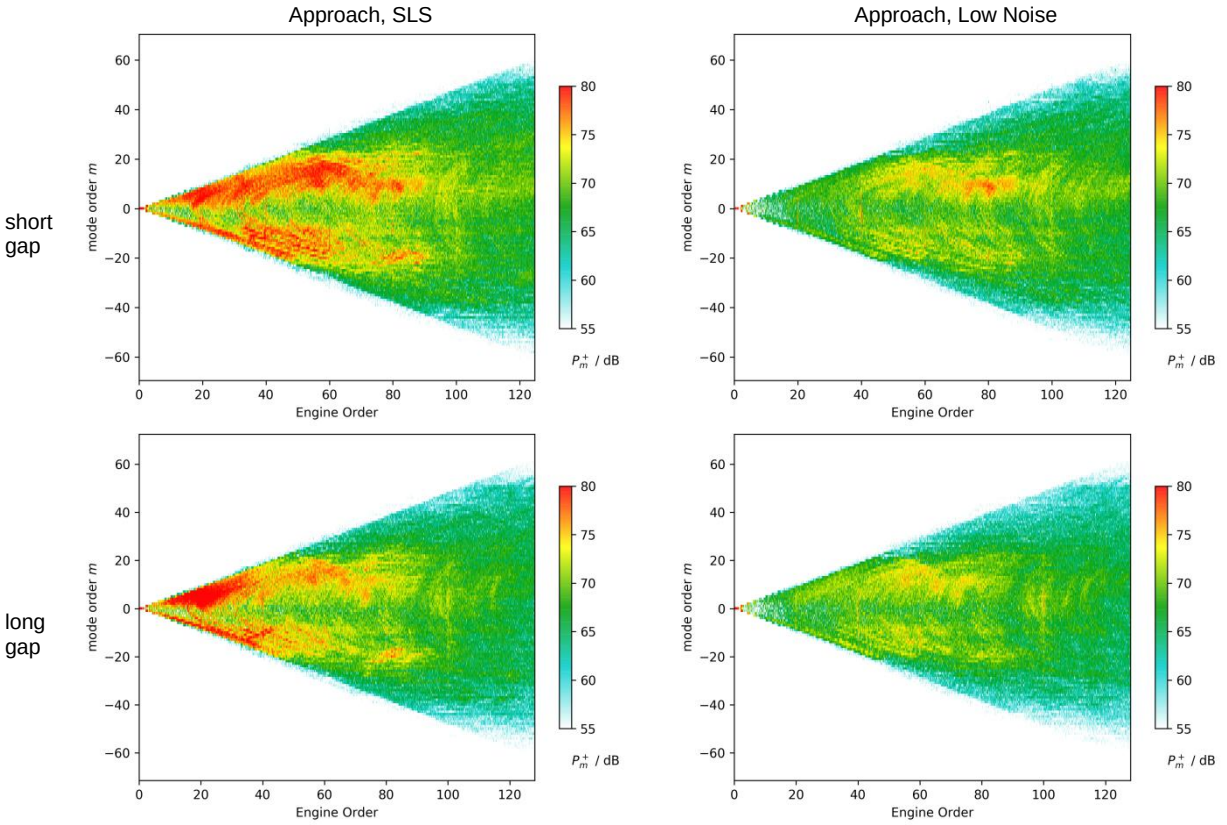

Figure 7: Impact of rotor-stator distance on sound power level of all downstream propagating modes (cumulated over all radial order, data is plotted as PSD in dB resp. 10^{-12} W/Hz).

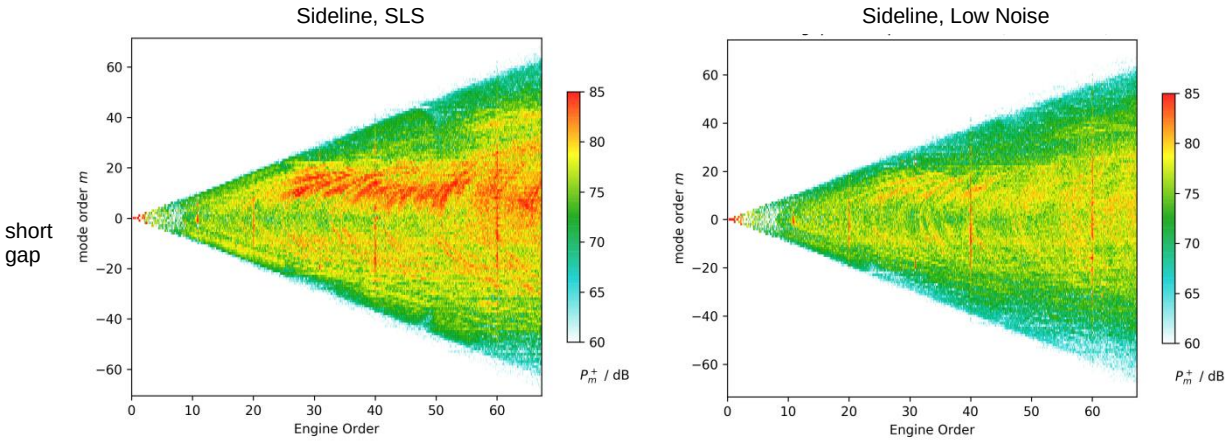

Figure 8: Impact of rotor-stator distance on sound power level of all downstream propagating modes (cumulated over all radial order, data is plotted as PSD in dB resp. 10-12 W/Hz).

VII. Appraisal of CAAS-RMA results

A. Impact of axial flow profile

The Impact of the boundary layer profile on the radial mode analysis results is studied for the operating points approach and sideline at SLS condition for the short gap configuration. In Figure 9 the boundary layer flow profiles in the RMA measurement section are depicted along with the mass flow equivalent plug flow.

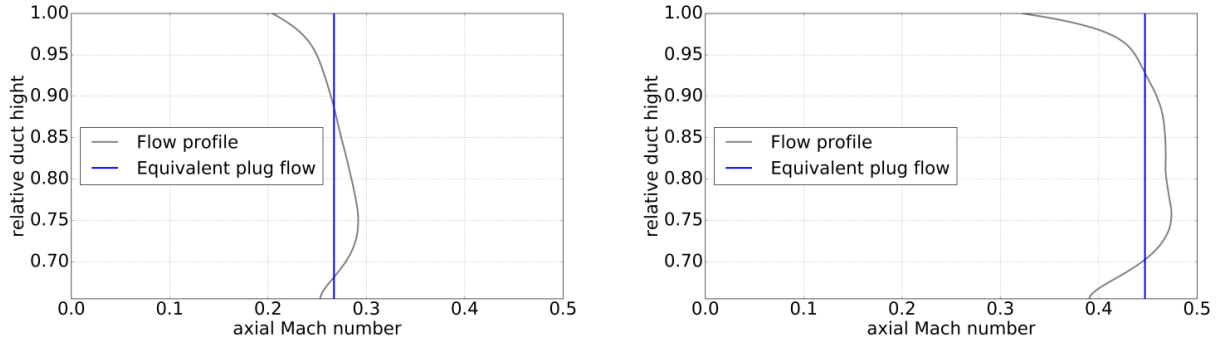

Figure 9: Flow profiles for approach (left) and sideline (right)

The different flow profiles result in different wave numbers and radial mode shape functions for the modal basis which is used in the RMA. At low azimuthal mode orders these differences are of the highest magnitude. Exemplarily the differences are plotted in Figure 10 for the azimuthal mode order m=1 and its radial mode orders versus the Helmholtz number. With increasing Helmholtz number the differences become larger. The trend of the differences also depends on the radial mode order. At the higher plug flow Mach number at the sideline operating condition the differences in the axial wave numbers are larger compared to the approach operating condition.

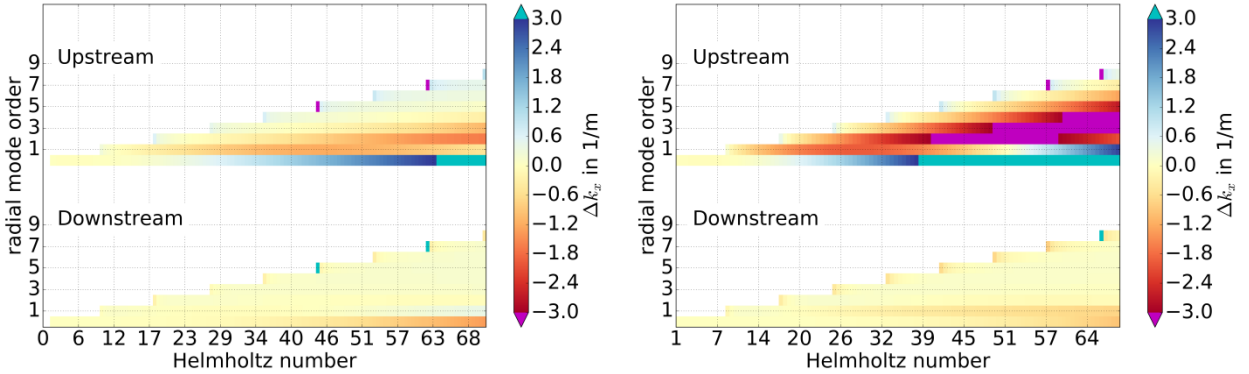

Figure 10: Differences in axial wave numbers (plug flow – boundary layer flow) for mode m=1, approach left, sideline right

The resulting differences in the sound power calculated by the RMA are shown in Figure 11 for the downstream and upstream propagation direction. An offset-like difference of the downstream sound power can be noticed form a low engine orders on up to the maximum analyzed engine order. The sound power is overestimated by the plug flow modal basis. At the sideline operating condition this overestimation amounts up to 2.5 dB and at approach up to 1 dB. The upstream propagating sound power shows a different characteristic. Here a good agreement is present up to higher engine orders (90 for approach, 40 for sideline). From there on a difference can be seen, which increases with frequency. This leads to a lower separation between the sound power of downstream and upstream propagating modes at higher frequencies for the analysis with consideration of the boundary layer profile.

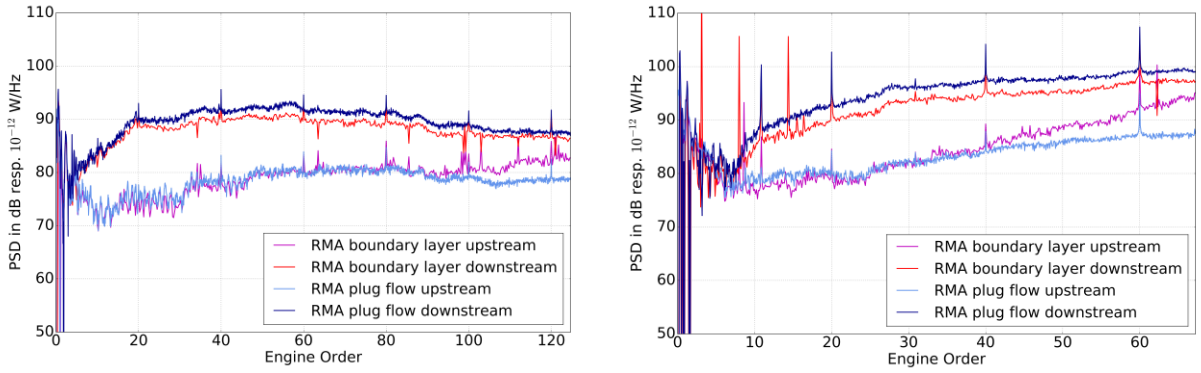

Figure 11: Influence of the modal basis on the calculated total sound power, approach left, sideline right

The deviations in the sound power due to different flow models are in the same magnitude as the deviations due to different analysis methods presented in following Section 8**Fehler! Verweisquelle konnte nicht gefunden werden.**. However these deviations cannot fully be explained by the discrepancy in the flow models, as they have a different characteristic and do not fully close the gap.

B. Reconstruction of mean sound pressure level

The radial mode breakdown, as described in paragraph III, is performed by matching a basis of radial mode eigenfunctions to the sound field measured by the spatially distributed sensors situated at the outer duct wall. The comparison of the reconstructed sound pressure level at the duct wall to the sound pressure spectrum averaged over the sensor array provides an evaluation of the stability and accuracy of the CAAS-method. Figure 12 presents the results for Approach and Sideline conditions. Both test points show a similar behavior. At low frequencies, where only few acoustic modes are cut-on and the turbulent pressure fluctuations dominate, as is found out by use of the WND method, the CAAS method does not account for all contributions to the total pressure signals recorded by the array. Above EO 20 for Approach condition and EO 25 for Sideline condition, the reconstructed spectra using the radial mode amplitudes from the CAAS-RMA method overestimate the measured averaged spectra. The difference between the spectra increases steadily towards high frequencies and yields approximately 4 dB at the maximum analyzed frequency. A possible explanation is found in the aforementioned limited accuracy of the EOMP-algorithm for the analysis of non-sparse azimuthal mode spectra in combination with the irregular sensor spacing of the CMD3 array. The inaccuracies occur for the computation of the individual azimuthal mode spectra at each axial position accumulating errors, which are subsequently distributed to all radial mode orders, if it is assumed that the errors are random.

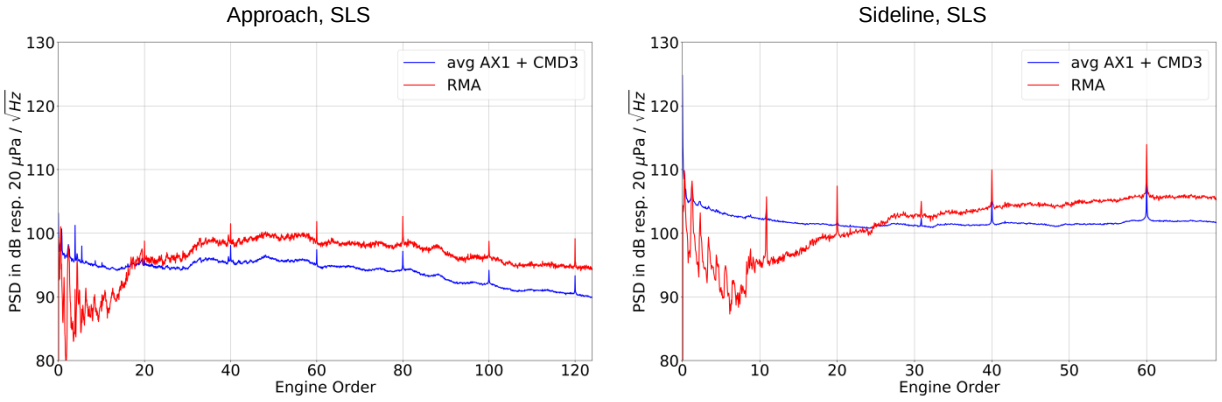

Figure 12: Overall reconstructed sound pressure level at the measurement section using the outcome of the CAAS-RMA method for short gap at two operating conditions in comparison to the average sound pressure spectrum detected by the sensors of the axial line and ring array.

VIII. Comparison of sound power estimations achieved by different mode analysis methods

The overall sound power transported by all modes in downstream respectively upstream direction is depicted in 3 for approach, cutback and sideline condition at SLS respectively Low Noise working line for the short fan gap configuration. The outcome of the CAAS-RMA method is compared with the estimations based on the WND analysis combined with the EEDM model. It should be noted that the displayed engine order ranges vary with the operating conditions. Both methods show the same trends for all cases. Generally is confirmed that the sound generation is lower at the Low Noise working line. However, the sound power levels determined with the CAAS method are consistently higher than estimated by the WND method. At Approach condition the difference amounts to 3 dB to 5 dB, at Sideline condition it varies between 5 dB and 8 dB. In the low frequency region the vulnerability of the CAAS method against turbulent pressure fluctuations becomes obvious. Also modes that are very close to their cut-on limits have a stronger effect on the analyses in this region due to low number of propagating modes at low frequencies But interestingly the width of the affected frequency bands is almost just half of the bandwidth, in which according to the diagrams of Figure 4 the turbulent pressure fluctuations dominate. Up to EO 40 the WND results indicate an increase for the reflected sound power close to the cut-on frequencies of higher radial mode orders. These details are not identified by the CAAS method, where considerable fluctuations of the sound power are found instead. Towards higher frequencies the variation of the sound power becomes narrower and is similar to the WND results.

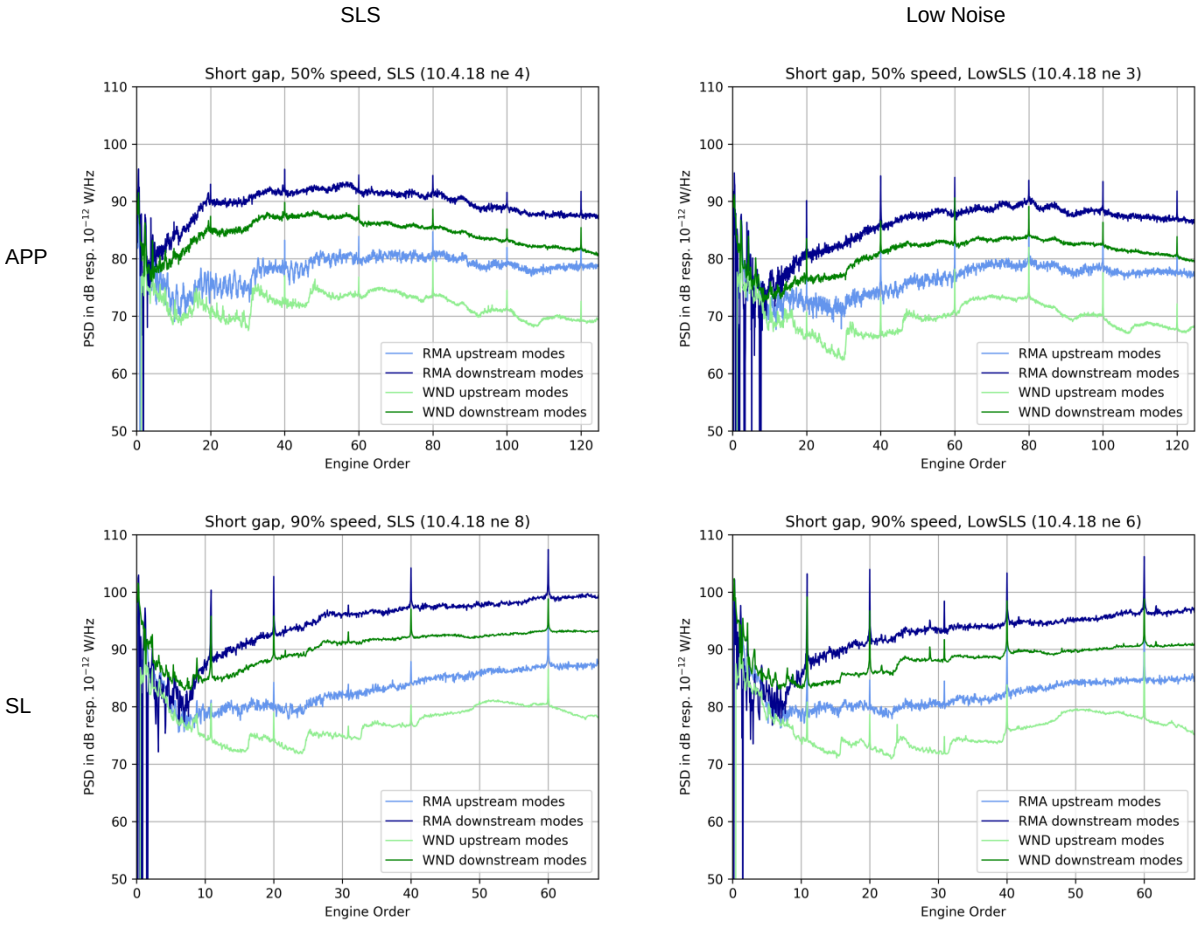

Figure 13: Overall sound power level of downstream and upstream propagating modes estimated with WND method respectively CAAS-RMA method for short gap at two working lines (data is plotted as PSD in dB resp. 10^{-12} W/Hz).

In Figure 14 the determined downstream radiated sound power is compared for the CAAS method and estimations based on the axial wave number decomposition resp. azimuthal mode decomposition (AMA). The outcome of the CAAS-RMA lies close to the WND results at low frequencies and approach towards the AMA estimation. This development indicates the general ability of the CAAS method to filter out turbulent pressure fluctuations. However, at SLS working line the sound power determined by the CAAS method yields higher levels than the other two methods, particularly at Approach condition. In contrast, the resulting sound power levels from the CAAS method and AMA are similar for both operating points at Low Noise working line.

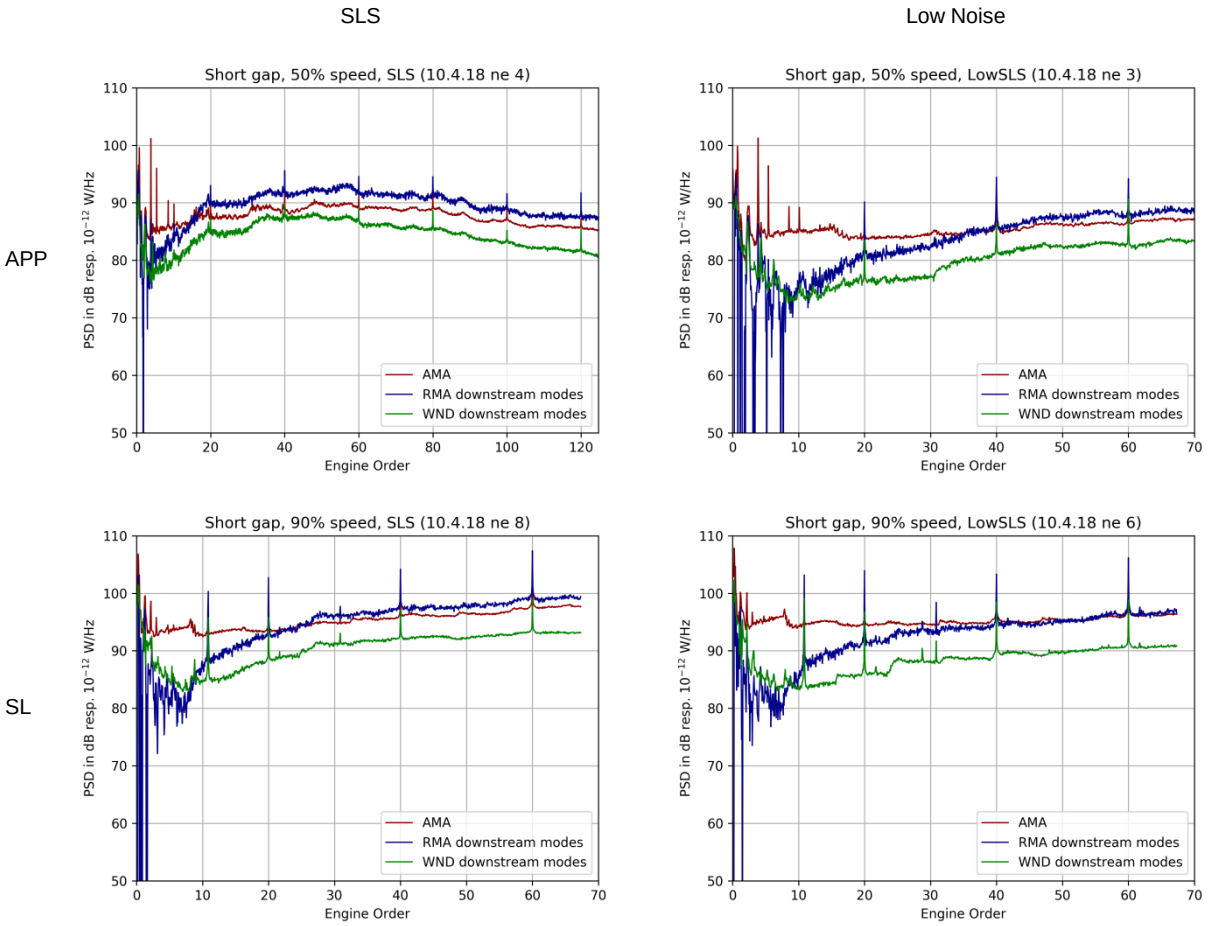

Figure 14: Overall sound power level of downstream propagating modes estimated with AMA method, WND method respectively CAAS-RMA method for short gap at two working lines (data is plotted as PSD in dB resp. 10-12 W/Hz).

IX. Conclusion and Outlook

The broadband sound field generated by the ACAT1 fan into the bypass is decomposed into its radial mode constituents up to frequencies kR=85 by application of the CAAS-RMA method to only 160 sensors. On the basis of the mode amplitudes the radiated sound power is calculated and compared to the outcome of sound power estimation techniques relying on single axial line or ring arrays in combination with the assumption of specific energy distribution among the radial mode orders. The axial line array is used for the wave number decomposition method (WND), which enables separating the turbulent pressure fluctuations from the downstream and upstream traveling acoustic components. Analyses are presented for two operating conditions (Approach and Sideline) at two different working lines. The comparison of the sound power results shows that the CAAS-RMA method yields higher sound power levels towards high frequencies in the order of 5 to 7 dB.

Different impacts on the CAAS-RMA analysis were assessed. The influence of superposed turbulent pressure fluctuations is limited to the low frequency domain, where the turbulent pressure fluctuations dominate the total sound pressure spectra at the outer duct wall, as identified by the WND method. At low frequencies, the sound power determined by the CAAS-RMA method is low in comparison to the other estimation techniques and exhibits strong fluctuations due to the small number of cut-on modes. The effect of the axial flow profile is investigated by accounting for the deviations of the radial mode shape functions and axial mode wave numbers due to the realistic flow profile in contrast to the typically assumed plug flow profile. In case of the realistic flow profile, the determined sound power is lower by 1 to 2.5 dB, but the sound power transported upstream increases strongly at high frequencies. The results indicate that accounting for the axial flow profile does not fully explain the differences between the CAAS-RMA method and the other estimation techniques. But it should be kept in mind that the estimation techniques base on simplified mode distributions and also rely on the assumption of a plug flow profile. However, in another verification step, i.e. the reconstruction of the measured sound pressure at the outer duct wall, an overshoot is found although with lower level and variation with frequency. This suggests that the CAAS-RMA derived mode amplitudes are at least partly overestimated, which might be linked to inaccuracies of the involved EOMP-algorithm.

The effect of the turbulent pressure fluctuations, of the axial flow profile and of the integrated signal analysis steps respectively the underlying sensor array design will be further investigated and quantified in future dedicated studies. Another issue will be the survey of the achieved radial mode breakdown with respect to the average energy distribution over the radial mode order in the interest of verification and improvement of existing models like the EEDM model.

X. Acknowledgement

The presented work was conducted in the frame of the project TurboNoiseBB, which has received funding from the European Union's Horizon 2020 research and innovation programme under grant agreement No. 690714.
The authors are very grateful to all the participants of to the test campaign, in particular Wolfram Hage (DLR), Karsten Liesner (AneCom AeroTest), the personal of AneCom AeroTest, Wolfgang Weith and Nick Crowder (Rolls-Royce), Azucena Pintado and Thomas Nodé-Langlois (AIRBUS).

References

[1] Tapken, U., Gutsche, D., and Enghardt, L., “Radial mode analysis of broadband noise in flow ducts using a combined axial and azimuthal sensor array," AIAA Aviation. 20th AIAA/CEAS Aeroacoustics Conference, 16.-20.06.2014, Atlanta, USA, No. AIAA 2014-3318, 2014.

[2] Tapken, U., Bauers, R., Neuhaus, L., Humphreys, N., Wilson, A., Stöhr, C., and Beutke, M., “A New Modular Fan Rig Noise Test and Radial Mode Detection Capability”, 17th AIAA/CEAS Aeroacoustics Conference, Portland, Oregon (USA), June 2011, pp. AIAA 2011-2897.

[3] Jürgens, W., Tapken, U., Pardowitz, B., Kausche, P., Bennett, G., and Enghardt, L., “Technique to Analyze Characteristics of Turbomachinery Broadband Noise Sources," 16th AIAA/CEAS Aeroacoustics Conference, 7-9 June 2010, Stockholm, Sweden, No. AIAA 2010-3979, 2010.

[4] Tapken, U., Gutsche, D., Enghardt, L., “Radial mode analysis of broadband noise in flow ducts using a combined axial and azimuthal sensor array," 20th AIAA/CEAS Aeroacoustics Conference, 16-20 June 2014, Atlanta, Georgia, USA, No. AIAA 2014-3318, 2014.

[5] Tapken, U., Pardowitz, B., Behn, M., “Radial mode analysis of fan broadband noise," AIAA Aviation Forum, 23th AIAA/CEAS Aeroacoustics Conference, 5-9 June 2017, Denver, Colorado, USA, No. AIAA 2017-3715, 2017.

[6] Dougherty, R. P., and Bozak, R., “Two-dimensional Modal Beamforming in Wavenumber Space for Duct Acoustics," AIAA Aviation Forum, 24th AIAA/CEAS Aeroacoustics Conference, 25-29 June 2018, Atlanta, Georgia, USA, No. AIAA 2018-2805, 2018.

[7] Bauers, R. and Tapken, U., “Separation of hydrodynamic perturbations in acoustic liner insertion loss measurements at a fan rig", 18th AIAA/CEAS Aeroacoustic Conference; 4-6 June 2012, Colorado Springs, CO, No. AIAA 2012-2277, 2012.

[8] Lowis, C., Joseph, P., and Kempton, A., “Estimation of the far-field directivity of broadband aeroengine fan noise using an in-duct axial microphone array", Journal of Sound and Vibration, Vol. 329, No. 19, 2010, pp. 3940-3957.

[9] Joseph, P., Morfey, C., and Lowis, C.: Multi-mode sound transmission in ducts with flow, Journal of Sound and Vibration, Vol. 264, 2003, pp. 523-544.

[10] Behn, Tapken, U., “Investigation of sound generation and transmission effects through an axial fan stage using Compressed Sensing-based mode analysis”, 25th AIAA/CEAS Aeroacoustics Conference, Delft, Netherlands, May 20-24, 2019

[11] R. Meyer, S. Hakansson, W. Hage, L. Enghardt, "Instantaneous flow field measurements in the interstage section between a fan and the outlet guiding vanes at different axial positions", Proceedings of 13th European Conference on Turbomachinery Fluid Dynamics and Thermodynamics, Lausanne, Switzerland, April 8-12, ETC2019-330, 2019

[12] Guérin, S., Kissner, C., Kajasa, B., Jaron, R., Behn, M., Hakansson, S., Pardowitz, B., Tapken, U., Meyer, R., Enghardt, L., "Predicting the trends in fan broadband noise measured for the ACAT 1 fan", 25th AIAA/CEAS Aeroacoustics Conference, Delft, Netherlands, May 20-24, 2019

[13] Kissner, C., Guérin, S., "Noise Prediction of the ACAT1 Fan Using a Three-Dimensional Random Particle Mesh Method", 25th AIAA/CEAS Aeroacoustics Conference, Delft, Netherlands, May 20-24, 2019

[14] Danny Lewis , Stéphane Moreau, Marc Jacob, "On the use of Large Eddy Simulations and analytical models to perform broadband rotor-stator interaction noise predictions", 25th AIAA/CEAS Aeroacoustics Conference, Delft, Netherlands, May 20-24, 2019

[15]Blazquez, R., Corral, R., "Efficient Fan Broadband Noise Prediction using Navier-Stokes Linearized Analysis", 25th AIAA/CEAS Aeroacoustics Conference, Delft, Netherlands, May 20-24, 2019

[16] Behn, M., Pardowitz, B., Tapken, U. "Separation of Tonal and Broadband Noise Components by Cyclostationary Analysis of the Modal Sound Field in a Low-speed Fan Test Rig", International Conference of Fan Noise, Aerodynamics, Applications and Systems, 18-20 April 2018, Darmstadt, Germany, Paper No. 43

[17] Mueller D., Schulz H-J., Zitouni G. and Baumann W., "Europe's Largest Aero Acoustic Test Facility for Aero-Engine Fans- the Development and Operation of the AneCom AeroTest Anechoic Chamber," AIAA-2005-3050, 11th AIAA/CEAS Aeroacoustics Conference, Monterey, 2005

[18] Lawson C., Hanson R.J., (1987), Solving Least Square Problems, SIAM

[19] Rademaker, E., Sijtsma, P., and Tester, B., "Mode detection with an optimised array in a model turbofan engine intake at varying shaft speeds", 7th AIAA/CEAS Aeroacoustics Conference, Maastricht, The Netherlands, May 2001, pp. AIAA 2001-2181.

[20] Kousen, K.A., "Pressure modes in ducted flows with swirl", 2nd AIAA/CEAS Aeroacoustics Conference, 6-8 May 1996, State College, Pennsylvania, USA, AIAA-1996-1679, 1996.

[21] Weckmüller, C., Hurst, J., Guérin, S., Enghardt, L., "Acoustic Eigenmodes for Ducted Sheared Mean Flow", AIAA Aviation, 20th AIAA/CEAS Aeroacoustics Conference, 16-20 June 2014, Atlanta, Georgia, USA, AIAA-2014-3117, 2014.

[22] Atassi, O.V., "Computing the sound power in non-uniform flow", Journal of Sound and Vibration, Vol. 266, 2003, pp. 75-92.

[23] Morfey, C.L., "Acoustic Energy in Non-Uniform Flows", Journal of Sound and Vibration, Vol. 14, No. 2, 1971, pp. 159-170.

[24] Antoni, J., "Cyclostationarity by examples," *Mechanical Systems and Signal Processing*, Vol. 23, 2009, pp. 987–1036.